

# The correction of systematic image deformations inherent to two-dimensional proportional counters

Mark N Kinnane<sup>1</sup>, Justin A Kimpton<sup>1</sup>, Martin D de Jonge<sup>1</sup>,  
Karoly Makonyi<sup>2,3</sup> and Christopher T Chantler<sup>1,4</sup>

<sup>1</sup> School of Physics, University of Melbourne, Victoria 3010, Australia

<sup>2</sup> National Institute of Standards and Technology, Gaithersburg, MD 20899, USA

Received 10 June 2005, in final form 26 August 2005

Published 4 October 2005

Online at [stacks.iop.org/MST/16/2280](http://stacks.iop.org/MST/16/2280)

## Abstract

Two-dimensional backgammon configuration and multiwire gas proportional counters have been in use for decades in the field of x-ray physics for high-precision or high-flux experiments. Systematics inherent to this type of detector lead to image distortions that are often overlooked or extremely difficult to quantify. They are usually seen as intrinsic to the detector performance, leading to loss of resolution, linearity and signal-to-noise ratio. This work presents the signature, cause and resolution of several key distortions. The physics of the breakdown between the anode and cathode, false event position reconstruction due to the electronic detector response, and the effect of asymmetric field lines between the anode and cathode are developed. The position resolution of these types of detectors is demonstrated to be comparable to a charge-coupled device when used in the same experimental configuration.

**Keywords:** x-ray beams, x-ray detectors, quantum electrodynamics, spectroscopy in atomic and molecular physics

## 1. Introduction

Multi-wire gas proportional counters (MWPC) have had a long history of use in the field of experimental optics since Charpak's development in 1968 [1, 2]. The charm quark and intermediate boson discoveries, which led to several Nobel prizes in particle physics, have particularly utilized these detector types [3–5]. This technology was rapidly applied to x-ray crystal diffraction and protein crystallography [6–8]. The versatility of this detector has also allowed extensive development in the fields of: x-ray spectroscopy [9, 10]; time-resolved studies in biological structures [11, 12]; and the study of synchrotron x-ray sources [13]. Some useful reviews of the development of the MWPC have been compiled [14, 15]. In recent times, the MWPC has been used for high-precision tests of quantum electro-dynamics in the x-ray regime using electron beam ion traps (EBITs) [10, 16].

Many variations on the basic idea of highly charged wires acting as a conduit for charge produced by ionization events have been implemented ranging from the earliest Geiger–Müller counters to the multiwire configuration of Charpak and the more modern microstrip detectors [17]. The recent popularity of charge-coupled devices (CCD) for two-dimensional x-ray event reconstruction is due to improved resolution resulting from reduced pixel size. However, the gas proportional counter has several advantages over CCDs: high photon detection efficiency over large energy ranges; individual photon, ‘event mode’ operation; and the cost effectiveness and simplicity of construction.

The x-ray optics group at the University of Melbourne [18] have constructed and tested a detector using the ‘Jeu de Jacquet’ or backgammon [19] configuration x-ray detector. The detector configurations (dimensions, gas type, wire thickness, etc) were based upon previous work [20–22], with several improvements which allowed a detailed investigation of the detector operation.

<sup>3</sup> Present address: Justus-Liebig-Universität Giessen, II, Physikalisches Institut, Giessen D-35392, Germany.

<sup>4</sup> Author to whom any correspondence should be addressed.

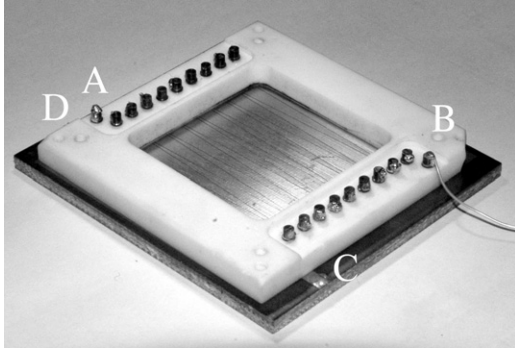


**Figure 1.** A detector anode wire and cathode board assembly. The anode wire runs between the 18 aligned pins. Two electrode pins ('A' and 'B') can be seen set back slightly from the others. One cathode board electrode connection can be seen protruding from beneath the anode assembly near the bottom of the image ('C'). The other electrode protrudes from the opposite side of the board ('D'). The white anode mounting board is 60 mm on an edge.

Previous work employing the backgammon-type detector has often overlooked, or been incapable of considering, particular systematic effects inherent to this type of detector. This work illustrates the cause, signature, and resolution of several systematic effects and compares the resulting resolution with a CCD camera, highlighting the capability of MWPCs to compete for a place in modern x-ray spectroscopy.

## 2. Detector and experiment

The shape and general description of backgammon detectors is given elsewhere [23]. The detector used for this work consisted of a  $6\ \mu\text{m}$  platinum wire wrapped around pins to create  $19 \times 50$  mm long segments spaced at 2 mm intervals and suspended half-way between a grounded nickel mesh and a  $40\ \text{mm} \times 40\ \text{mm}$  backgammon-type cathode board (figure 1). The cathode board was constructed from a printed circuit board with a pitch of  $2\ \text{mm} \times 48\ \text{mm}$ . The gap between the mesh and backgammon board was 10 mm. The detector components were contained within a sealed chamber filled with 90% Ar/10%CH<sub>4</sub> (P10) to a pressure of 1.25 atmospheres. The wire was kept at a positive bias of +2150 V dc. The mesh, cathode board and body were grounded to earth. The effective area of the detector ( $855\ \text{mm}^2$ ) was determined by a circular entrance window with a diameter of 33 mm.

Four charge-induced signals were recorded by the detector system, two from the positively charged wire electrodes and two from the grounded cathode board electrodes. The signal amplitudes were proportional to the amount of charge received by each electrode. The signals generated by the detector for each event were passed from a set of charge-coupled pre-amplifiers through signal conditioning amplifiers to a discriminator/coincidence circuit, required to ensure that the four signals originated from the same event. If the signals met the criteria for a coincident event the signal amplitudes were digitized (to a 13-bit precision) and passed to the controller computer for processing. The electronics filtered out signals that were above 5 V in amplitude. The digitized values were used to determine the position at which charge collection

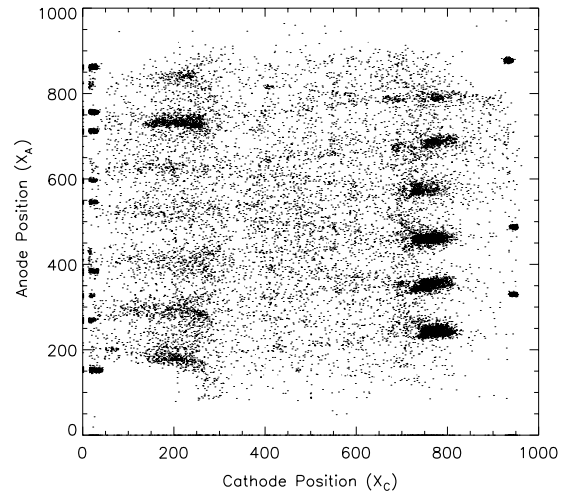


**Figure 2.** Two-dimensional spectrum of  $X_A$  versus  $X_C$  for a raw image after irradiation by He-like Ti 1s–2p x-rays. Each point represents one event. Note the high density regions at cathode positions 20, 240, 750 and 970. These regions lie at the turning points of a sawtooth pattern corresponding to the reconstructed path of the anode wire. The He-like Ti spectral lines which run vertically between the cathode positions 400 and 750 are, in this spectrum, almost indistinguishable from the background.

occurred. The relative position along the anode wire could be reconstructed using

$$R_A = \frac{A}{A + B}, \quad (1)$$

where  $A$  and  $B$  were the anode signal amplitudes, in volts, after amplification and digitization. The relative position across the cathode board could be reconstructed using

$$R_C = \frac{C}{C + D}, \quad (2)$$

where  $C$  and  $D$  were the cathode signal amplitudes, in volts, after amplification and digitization. The analysis (and subsequent plots below) defined anode position and cathode position respectively as

$$X_A = R_A \times 1000, \quad (3)$$

and

$$X_C = R_C \times 1000, \quad (4)$$

where each position was binned into 1000 channels. The images were then composed of  $1000 \times 1000$  channels.

A key development of this experiment over previous work involving backgammon-type detectors was the independent event-mode recording of each of the four signal amplitudes  $A$ ,  $B$ ,  $C$  and  $D$  rather than just the (scaled and binned) position ratios  $X_A$  and  $X_C$ . The following section presents our use of event-mode counts to remove systematic effects inherent to the backgammon (and related) detector types.

## 3. Raw images

The  $X_A$  versus  $X_C$  two-dimensional spectra shown in figures 2 and 3, obtained from the helium-like titanium 1s–2p and the chromium  $K\beta$  transitions respectively, are representative of data collected from an EBIT source and a fluorescent source.

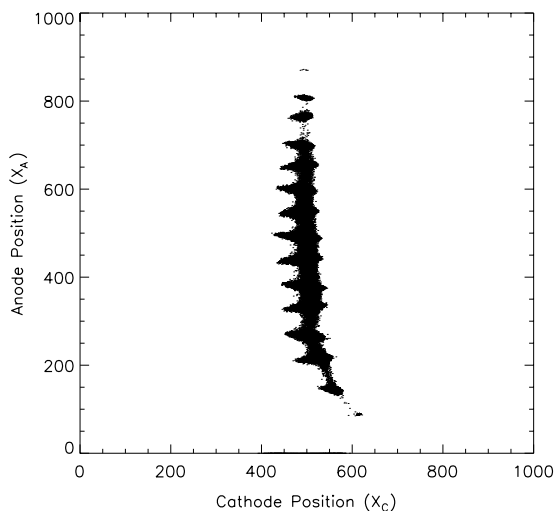


**Figure 3.** Two-dimensional spectrum of  $X_A$  versus  $X_C$  for a raw image after irradiation by Cr  $K\beta$  x-rays and diffraction by a dispersive curved Ge 220 crystal. The dispersion axis for energy is in the horizontal plane. Note the curvature of the line at the lower portion of the image.

The low flux He-like Ti spectrum (of order  $0.1 \text{ counts s}^{-1}$ ) was recorded over 6 h whereas the high flux Cr  $K\beta$  spectrum (of order  $2000 \text{ counts s}^{-1}$ ) was recorded in 10 min. Due to background count rates, the longer count time results in the noisier appearance of the He-like Ti spectrum.

Two significant artefacts are observed in these spectra. The He-like Ti data (figure 2) contain regions of anomalously high count density centred around the cathode channels 20, 240, 750 and 970. These regions extend over the entire anode range and occur at the wire turning points (the sharp points of a sawtooth pattern) which is consistent with arcing between the anode wire mounting pins and the grounded cathode board.

The lines in both spectra were expected to have a slight bow due to the anticlastic curvature of the monochromating crystal [24, 25]. Figure 3 clearly shows a distinct left-to-right curvature at the lower end of the detector face. However, this level of curvature is much too large to be due to the crystal and is attributed to an asymmetric electric field between the wire and board.

Figure 4 shows signal strength ( $S_C$ ) versus the cathode position ( $X_C$ ) for the He-like Ti spectrum in figure 2. The signal strength is proportional to the total charge collected by the anode or cathode and is defined as

$$S_A = A + B, \quad (5)$$

and

$$S_C = C + D, \quad (6)$$

for the anode and cathode, respectively.

This signal strength spectrum contains significant structure. The spectral lines and arcing lines flare away from a central point on the cathode axis. The magnitude of this flare is dependent upon the signal strength. The lines of this plot would be straight if signal strength had no bearing on the position of the reconstructed photon events. The curvature of the lines is a cause for concern as this effect is manifest as a broadening of the spectral lines in figures 2 and 3 when projected onto the cathode axis. This work demonstrates that

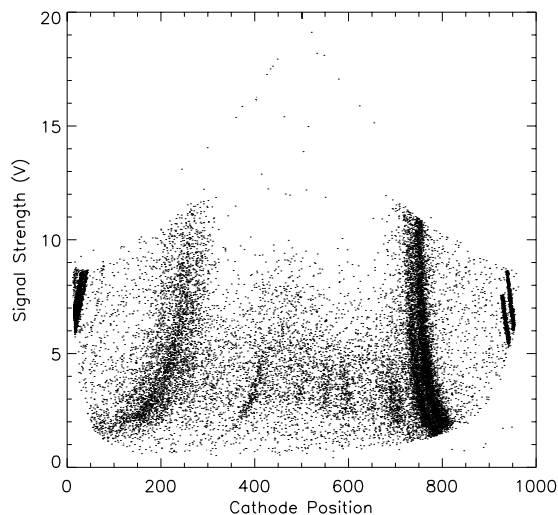


**Figure 4.** Signal strength ( $S_C$ ) versus cathode position ( $X_C$ ) for the He-like Ti  $1s-2p$  transition following diffraction by a dispersive curved Ge 220 crystal. The teardrop-shaped event envelope is due to the upper and lower level discriminator settings in the signal-processing electronics. The flaring of the lines observed towards the bottom of this figure is due to ‘unbalanced’ electronic channels.

this curvature is due to the signal-processing electronics and to the use of unbalanced signal gain settings for a pair of delay amplifiers.

## 4. Key signatures

### 4.1. Removal of spurious arcing events

For correct operation of any MWPC, the positive potential of the anode wire relative to the grounded cathode board must be set such that the detector behaves as a proportional counter. Our preliminary studies found that the optimum bias voltage for the detector to remain in the proportional regime was +2150 V dc. Breakdown was observed if the voltage was set above +2600 V dc, indicated by particularly dense regions of events on the image despite the detector being uniformly illuminated by a test source or completely shielded from x-rays.

Regions of higher density counts were observed near the edges of the detector during long exposure times, such as shown in figure 2 for the He-like Ti spectra. These do not correspond to the predicted position of the spectral lines. Despite the bias being set to the proportional regime, this was a clear indication of breakdown. These dense regions fall at the turning points of the sawtooth, shown in figure 2, the peaks of which represent the position of the mount pins. Sharp points on solder beads at the pins, used to retain tension in the anode wire, caused charge accumulation leading to regions of high electric field. The regions of high electric field caused self-induced gas ionization and arcing events between the pins and the cathode board.

For data collection rates of order 100 Hz or higher this phenomenon is completely dominated by normal events so that the effect is unobservable. However during low-flux operation (less than 1 Hz) these ‘rare’ events have a significant impact on the overall result. Accordingly, the arcing signal is not apparent in the fluorescent-source spectrum of figure 3.

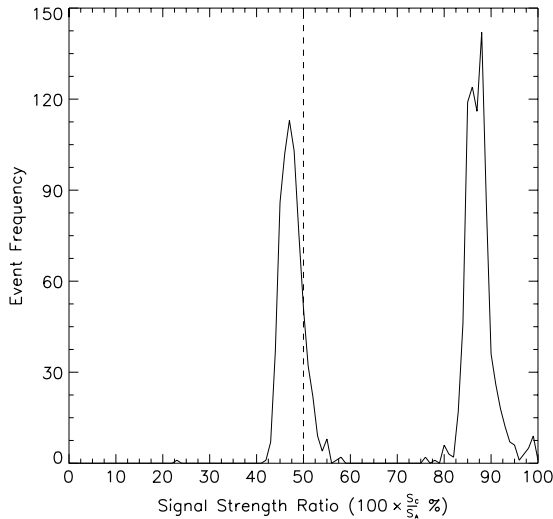


**Figure 5.** Frequency histogram of the cathode signal strength  $S_C$  as a percentage of the anode signal strength  $S_A$  ( $100 \times \frac{S_C}{S_A} \%$ ) for a portion of the events shown in figure 2. Two clearly resolved distributions are obtained: the left-hand peak represents x-ray events and the right-hand peak represents arcing events.

The charge avalanche caused by an incident photon develops close to and around the wire [26], and the positive ions can travel to the grounded cathode board or to the grounded nickel mesh with equal probability. Therefore the cathode board signal strength  $S_C$  should be approximately 50% of the anode wire signal strength  $S_A$  [21]. Conversely, arcing events could occur between the wire assembly and the grounded chamber (approaching 0% signal strength ratio and no coincident signals) or between the wire assembly and the cathode board (approaching 100% signal strength ratio). Figure 5 shows the ratio of signal strengths  $\frac{S_C}{S_A}$  for a portion of He-like Ti data. The spurious counts are identified as those with signal strength ratios of about 90%, clearly indicating the cause of these events to be breakdown between the wire and board. The distributions are not exactly 50% and 100%, indicating some loss of the positive ions due to electronic recombination in the charge collection.

The widths of the distributions for each type of event, x-ray and arcing, were very narrow in comparison to their separation, therefore allowing clear identification and labelling of their physical origin. By taking the signal strength ratio of each event, we have ‘cleaned’ the spectrum, thus removing all regions of high density events from figure 2, with no loss of actual x-ray events and with no effect on the reconstructed positions.

#### 4.2. Correction of image distortion due to electronic response

The reconstructed event position should depend only on the position of the photon–gas interaction location and subsequent charge deposition. Therefore, a plot of signal strength ( $S_C$ ) versus cathode position ( $X_C$ ) for a set of spectral lines running perpendicular to the wire segments should ideally result in a series of vertical lines each centred on the spectral line centroids.

It is important that the electronic response during the passage of the signal from the detector to the controlling

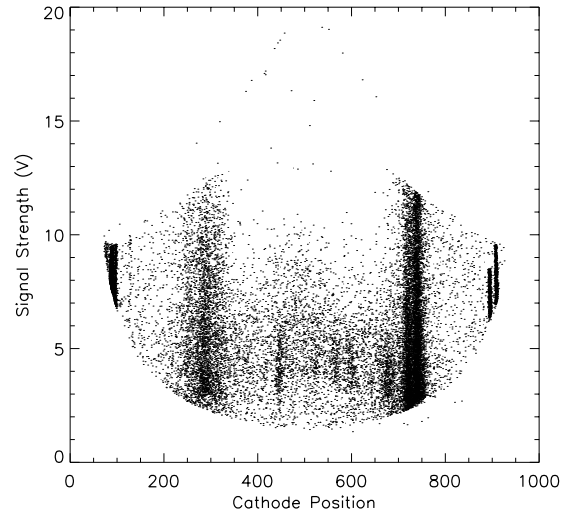


**Figure 6.** Signal strength ( $S_C$ ) versus cathode position ( $X_C$ ) for the He-like Ti 1s–2p transition following diffraction by a dispersive curved Ge 220 crystal. The flaring of the lines observed towards the bottom of figure 4 has been removed. Arcing events are still present but x-ray spectral lines (four lines between cathode positions 450 and 700) are clearer.

computer has a minimal effect on the relative signal strengths. However, the electronic response of the processing circuitry, in particular a set of delay amplifiers, added unequal offsets of  $-(650 \pm 40)$  mV dc and  $-(400 \pm 40)$  mV dc to the cathode signals,  $C$  and  $D$ , respectively.

Figure 4 shows that the lines flared away from some central point of the cathode board, with the magnitude of the shift strongly dependent on the signal strength. This flaring is due to the offsets added during the signal processing. The corrected cathode position ratio (equation (2)) was

$$R_C = \frac{C + \gamma}{C + D + \gamma + \delta} \quad (7)$$

where  $C \rightarrow C + \gamma$  and  $D \rightarrow D + \delta$ , and  $\gamma$  and  $\delta$  were the offsets of each signal amplitude.

The values of  $\gamma$  and  $\delta$  were modelled using a finite difference method, which involved finding the values which gave the maximum change in the shape of the spectrum created, by projecting figure 4 onto the cathode position axis. Values of  $\gamma = (571 \pm 40)$  mV and  $\delta = (352 \pm 15)$  mV gave the optimal fit.

The ratio between these numerically derived offsets and the ratio of the delay amplifier above fell within error of one another confirming that the flaring was due to a constant offset in the electronic response. Figure 6 shows signal strength ( $S_C$ ) versus the cathode position ( $X_C$ ) for a He-like Ti spectrum after the offsets have been removed.

This effect is inherent to this detector type and is due to the electronic processing. It will always be present, and is quite dangerous if only the positions  $X_A$  and  $X_C$  are recorded—it manifests itself as an asymmetric broadening, and hence an asymmetric shift of the centroids of spectral lines. Further, the magnitude of the effect *cannot* be determined if only  $X_A$  and  $X_C$  are recorded.

The work presented here demonstrates that even if the effect is relatively large it can easily be corrected for to almost arbitrary precision (and with minimal or negligible loss of

signal) if *and only if* each of the four signal amplitudes are recorded.

#### 4.3. Straightening of the spectral line curvature due to electric field distortion

A key feature of figure 3 is an overall curvature in the spectral line. The offsets of the electric response described above manifest themselves as spectral line broadening—not spectral line curvature. The cause of the curvature could not be attributed to an effect of the electronic response on the signal amplitudes.

The spectrometer used for this work was a Johann-type curved crystal spectrometer [27]. A test of the detector using a slit aperture with flat-field illumination directly confirmed that the image curvature was not due to the crystal, and we dismiss this as a significant cause.

Small wiggles in spectral lines are regularly observed with this type of detector due to the nonuniformity of the backgammon teeth; however, the magnitude of these is less than 1% of the absolute position of the spectral line on the detector face [22]. The curvature of the spectral lines is observed to be 20%–30% of the absolute cathode position. This large curvature indicates an asymmetry in the electromagnetic field lines between the anode wire and cathode board, which determines the path of an induced charge cloud. Much work has been done on modelling the fields inside these detectors [28–30], however, the effects of asymmetry can generally only be observed indirectly by studying and modelling results.

The model for spatial reconstruction, presented below, assumes that the spectral line incident upon the detector face was straight and aligned perpendicular to the detector wire segments. Any curvature or misalignment of the reconstructed line is therefore due to systematic effects within the detector.

The precise location of a spectral line on the detector face was found by creating a 1000 × 1000 channel two-dimensional histogram of the reconstructed x-ray event positions.

Several fits were performed on a number of spectral lines recorded at different times and positions on the detector in an extensive data set. The curvature of a spectral line was modelled using a quartic function of the form

$$X_C = \phi X_A^4 + \varphi X_A^3 + \chi X_A^2 + \psi X_A + \omega \quad (8)$$

where  $X_C$  represents the cathode position,  $X_A$  represents the anode position, and the fitting procedure provided values for  $\phi$ ,  $\varphi$ ,  $\chi$ ,  $\psi$  and  $\omega$ . As the curvature varied with cathode position, the coefficients of equation (8) were modelled as linear functions of the cathode position at which the spectral line crossed the central wire ( $X_W$ ). The central wire was considered to be least affected by asymmetry in the electric field and hence was considered to truly represent the spectral line positions. The equations for the coefficients as functions of  $X_W$  were

$$\phi = -1.225 \times 10^{-11}(X_W) - 7.457 \times 10^{-9} \quad (9)$$

$$\varphi = 2.647 \times 10^{-8}(X_W) - 1.640 \times 10^{-5} \quad (10)$$

$$\chi = -2.111 \times 10^{-5}(X_W) - 1.300 \times 10^{-2} \quad (11)$$

$$\psi = 7.250 \times 10^{-3}(X_W) - 4.711 \quad (12)$$

$$\omega = 1.140 \times 10^{-1}(X_W) + 599.978. \quad (13)$$

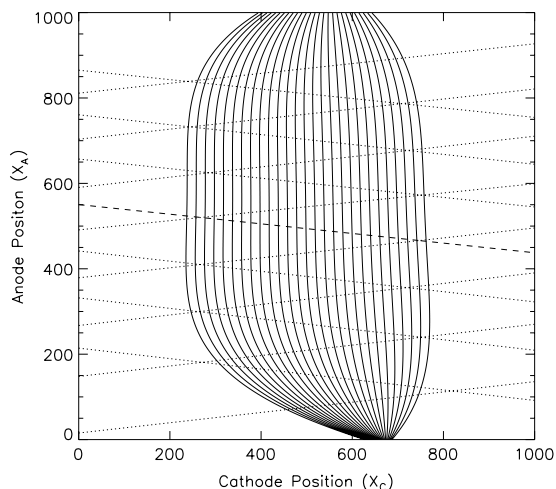


**Figure 7.**  $X_A$  versus  $X_C$  for a model for 26 simulated straight spectral lines with a *central wire* crossing point separation of 20 channels. Dotted lines represent the wire positions over the detector face. The *central wire* ( $X_W$ ) is indicated by the dashed line.

Figure 7 illustrates the results of this model for an abstract array of 26 straight spectral lines with a central wire crossing-point separation of 20 channels. After inversion, this model straightened the curvature of calibration source spectral lines vertically to less than 5 channels in 1000.

Asymmetry in the electric field near the edges will always be an issue for this type of detector, given the shape of the high potential components (wires and pins). This potential asymmetry, coupled with high potentials at solder points, can give rise to severe distortion of any spectral lines due to the shifting of the charge clouds. This work demonstrates that these distortions can be corrected to high accuracy using the model presented, even if the distortion is large (of order 20% of the absolute cathode position).

## 5. Application of corrections

Figures 8 and 9 show the effects of removing the above systematics from measurements of vanadium  $K\alpha$  spectral lines. A one-dimensional spectrum was taken by projecting the two-dimensional spectrum onto the cathode axis. The effect of removing the arcing counts from the fluorescent source data was unobservable by eye and is not shown separately.

A dramatic improvement in the resolution of the spectral peaks was achieved as each systematic was removed. The  $K\alpha_1$  peak (the right-hand peak) position in figures 8 and 9 is shifted from channel 533 to 553 and the full width at half maximum is reduced from 32 channels to 16 channels. For wavelength dispersive spectrometry and calibration the most serious effect of failing to correct for these systematics is the shift in the positions of the peak centroids.

A CCD camera was used in place of the backgammon detector on the spectrometer to test the resolution of the characteristic spectral lines provided by the fluorescent source. The CCD pixel size was 20  $\mu\text{m}$ . Figure 10 shows the resulting V  $K\alpha$  spectrum with a 10 min exposure time. The peak-to-trough ratio ( $K\alpha_1$  height to the minimum between  $K\alpha$  peaks) was taken as a measure of resolution. The ratio for the CCD camera was approximately 5 and the ratio

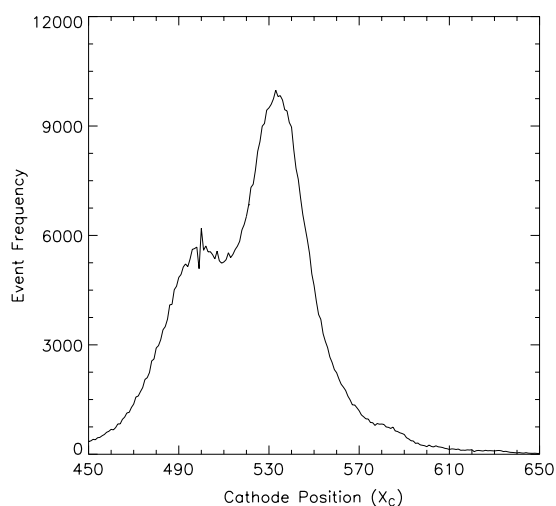


**Figure 8.** Raw  $V K\alpha$  spectrum prior to correction. This spectrum was created by projecting the raw position data onto the cathode position ( $X_C$ ) axis.

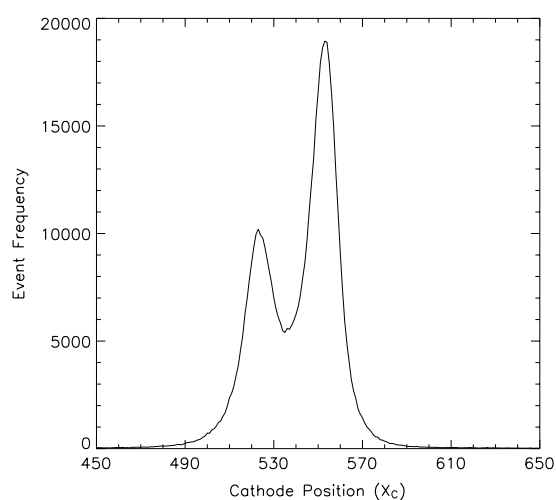


**Figure 9.**  $V K\alpha$  spectrum after the calibration and correction for flaring and curvature effects. This spectrum was created by adding the offset values of  $\gamma = 571$  mV and  $\delta = 352$  mV to the  $C$  and  $D$  values respectively and then inverting the quartic curve using the above model before projecting onto the cathode position ( $X_C$ ) axis.

for the backgammon was approximately 3.8. Both spectra are slightly vignettted due to a minor misalignment of the crystal. The ability of the backgammon system to record and label individual photon events allowed the investigation of spectrometer-related systematics *not possible* with the CCD camera (i.e. a mechanical drift in the detector position, short-term variations in x-ray flux) [10, 16, 31].

## 6. Discussion

The procedures described in this paper can be used to linearize scaling deformations and other detector nonlinearities in a relatively straightforward manner. This allows the ideal detector performance to be approached closely even in the presence of a non-optimum response function. Note however that in all cases an appropriate uncertainty should be robustly propagated throughout the analysis.

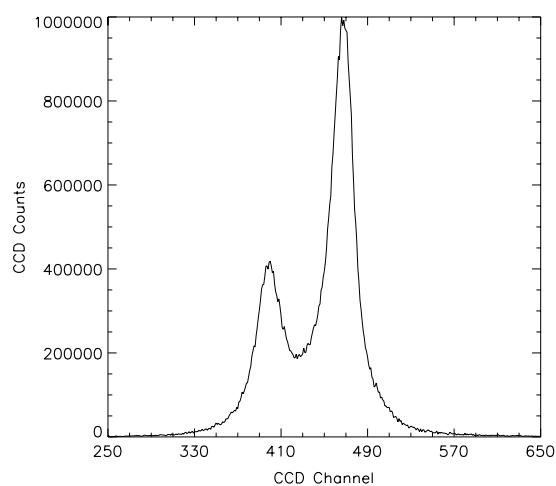


**Figure 10.** Image of  $V K\alpha$  spectrum recorded with a CCD camera over 10 min. Similar resolution was achieved with the CCD camera when used in place of the backgammon detector. Note that counts are CCD counts and not individual photon events.

Some of these signatures of errors might appear straightforward. It is well known that high voltages will cause arcing, and that the presence of sharp points will concentrate the field lines. The key issue here is how to find the cause of a series of systematics, and the level at which the cause or problem impacts upon the recovered data. All detectors have nonlinearities, and these must be diagnosed and calibrated for (with known uncertainties) before useful measurements can be reported. Mutual capacitance and electronic cross-talk between wire segments, cathode sections or amplifiers lead to similar positional readout errors or nonlinearities and must in general be diagnosed and calibrated [15, 32].

Electric field distortion can be a large or small effect and lead to significant nonlinearities. Nonetheless, this is a common feature of multi-wire proportional counters and is often a critical specification (or limitation) of the devices [33]. In figure 6 of Smith [33], the central region has 2% differential nonlinearity and 20% or so near the edges, in consonance with the measurements obtained in this study. Although the linearization and calibration reported here was certainly complex, it resulted in a perfect performance of the detector without a significant (1%) loss of signal or resolution. As such the concerns of this paper not only address key issues for the development of backgammon detectors, but also address wider concerns of multi-wire ion chambers and micro-strip detectors. In this way, we hope to show that detailed event-mode signal processing has key advantages over common prior approaches to detector processing.

## 7. Conclusion

This work has highlighted, and provided solutions for, several key systematics often overlooked when using backgammon configuration MWPCs. The solutions presented here can be applied equally to many other MWPC configurations in which the same causes of image distortion occur. This work has also provided further evidence of the ability to obtain position information comparable to more modern detectors and thus

provides an incentive to further improve currently available MWPC technology.

## Acknowledgments

The authors would like to thank G Christodoulou and L Hudson for support with the experimental work. We gratefully acknowledge helpful discussions with A Henins.

## References

- [1] Charpak G, Bouclier R, Bressani T, Favier J and Zupancic C 1968 *Nucl. Instrum. Methods* **62** 262
- [2] Charpak G, Rahm D and Steiner H 1970 *Nucl. Instrum. Methods* **80** 13
- [3] Charpak G 1970 *Ann. Rev. Nucl. Sci.* **20** 195–254
- [4] Richter B 1977 *Rev. Mod. Phys.* **49** 251–66
- [5] Rubbia C 1985 *Rev. Mod. Phys.* **57** 699–722
- [6] Cork C, Fehr D, Hamlin R, Vernon W, Xuong Ng H and Perez-Mendez V 1974 *J. Appl. Cryst.* **7** 319–23
- [7] Cork C, Hamlin R, Vernon W and Xuong Ng H 1975 *Acta Cryst. A* **31** 702–3
- [8] Poe M, Greenfield N J, Hirschfield J M, Williams M N and Hoogsteen K 1972 *Biochemistry* **11** 1023–30
- [9] Ito S, Tosaki M, Maeda N, Takahashi N, Katano R and Isozumi Y 1993 *Nucl. Instrum. Methods B* **75** 112–5
- [10] Chantler C T, Paterson D, Hudson L T, Serpa F G, Gillaspay J D and Takacs E 1999 *Phys. Scr. T* **80** 440–2
- [11] Faruqi A R and Huxley H E 1981 *Scattering Techniques Applied to Supramolecular and Nonequilibrium Systems* (New York: Plenum) p 201
- [12] Irving M, Lombardi V, Piazzesi G and Ferenczi M 1992 *Nature* **357** 156–8
- [13] Fischer J, Radeka V and Smith G C 1986 *Nucl. Instrum. Methods A* **246** 511–6
- [14] Charpak G 1977 *Nature* **270** 479–82
- [15] Charpak G and Sauli F 1984 *Ann. Rev. Nucl. Part. Sci.* **34** 285–349
- [16] Chantler C T, Paterson D, Hudson L T, Serpa F G, Gillaspay J D and Takacs E 2000 *Phys. Rev. A* **62** 042501–1
- [17] Heijne E H M, Hubbeling L, Hyams B D, Jarron P, Lazyeras P, Piuz F, Vermeulen J C and Wylie A 1980 *Nucl. Instrum. Methods* **178** 331–43
- [18] Paterson D 1999 *PhD Thesis* The University of Melbourne
- [19] Allemand R and Thomas G 1976 *Nucl. Instrum. Methods* **137** 141
- [20] Mizogawa T, Awaya Y, Isozumi Y, Katano R, Ito S and Maeda N 1992 *Nucl. Instrum. Methods A* **312** 547–52
- [21] Duval B P, Barth J, Deslattes R D, Henins A and Luther G G 1984 *Nucl. Instrum. Methods* **222** 274
- [22] Luther G G, Cowan P L, Henins A and Brennan S 1986 *Nucl. Instrum. Methods A* **246** 537
- [23] Chantler C T *et al* 2005 in preparation
- [24] Yang W, Larson B C, Ice G E, Tischler J Z, Budai J D, Chung K-S and Lowe W P 2003 *Appl. Phys. Lett.* **82** 3856–8
- [25] Ferrer J-L 1999 *Nucl. Instrum. Methods A* **431** 224–33
- [26] Zhong Z, Kao C C, Siddons D P and Hastings J B 2001 *J. Appl. Cryst.* **34** 646–53
- [27] Sauli F 1987 *Experimental Techniques in High Energy Physics* (Reading, MA: Addison-Wesley) pp 126–30
- [28] Johann H H 1931 *Z. Phys.* **69** 185
- [29] Charpak G, Petersen G, Policarpo A and Sauli F 1978 *Nucl. Instrum. Methods* **148** 471
- [30] Erskine G A 1972 *Nucl. Instrum. Methods* **105** 565
- [31] Erskine G A 1982 *Nucl. Instrum. Methods* **198** 325–36
- [32] Chantler C T, Paterson D, Hudson L T, Serpa F G, Gillaspay J D and Takacs E 1999 *Phys. Scr. T* **80** 440–2
- [33] Piuz F, Roosen R and Timmermans J 1982 *Nucl. Instrum. Methods* **196** 451
- [34] Smith G C 1984 *Nucl. Instrum. Methods* **222** 230–7